Available online at www.sciencedirect.com
SCIENCE DIRECT®
Journal of Computational Physics 198 (2004) 450–468
JOURNAL OF COMPUTATIONAL PHYSICS
www.elsevier.com/locate/jcp

A phase field approach in the numerical study of the elastic bending energy for vesicle membranes ☆

Qiang Du *, Chun Liu, Xiaoqiang Wang

Department of Mathematics, Pennsylvania State University, 218 McAllister Building, University Park, PA 16802, USA

Received 29 July 2003; received in revised form 13 January 2004; accepted 20 January 2004
Available online 26 February 2004

Abstract

In this paper, we compute the equilibrium configurations of a vesicle membrane under elastic bending energy, with prescribed volume and surface area. A variational phase field method is developed for such a problem. Discrete finite difference approximations and numerical simulations are carried out in the axial symmetrical cases. Different energetic bifurcation phenomena are discussed.

Keywords: Phase field; Elastic bending energy; Bio-membrane; Finite difference methods; Numerical simulation; Axial-symmetry; Bifurcation diagram

1. Introduction

Recently, there have been many experimental and analytic studies on the configurations and deformations of elastic bio-membranes [7,17,32,36,38,39]. In this paper, we study the shape transformation of a single component vesicle, using a phase field approach. While our goal is to study the deformation and interaction of such vesicles under various external fields, such as the flow fields or electric fields, here we first focus on the fundamentals of the phase field formulation and its numerical approximations in the absence of the applied fields.

The usual single component vesicles are formed by certain amphiphilic molecules assembled in water to build bilayers. They are the simplest models for the biological cells and molecules. The equilibrium shape of such an membrane is determined by the shape energy. In the isotropic case, it usually consists the following bending energy [10,11]:

☆ The research of Q. Du and X. Wang is supported in part by NSF-DMS 0196522 and NSF-ITR 0205232. The research of C. Liu is supported in part by American Chemical Society.
* Corresponding author. Tel.: +814-8653674; fax: +814-8653735.
E-mail addresses: qdu@leibniz.math.psu.edu, qdu@math.psu.edu (Q. Du), liu@math.psu.edu (C. Liu), wang@math.psu.edu (X. Wang).

0021-9991/$ - see front matter
doi:10.1016/j.jcp.2004.01.029

$$E_{\text{elastic}} = \int_{\Gamma} \frac{k}{2} H^2 \, \mathrm{d}s, \tag{1.1}$$

where $H = (k_1 + k_2)/2$ is the mean curvature of the membrane surface, with k_1 and k_2 as the principle curvatures. The parameter k is the bending rigidity, which can depend on the local heterogeneous concentration of the species (such as protein molecules on the blood cells). The bending energy given above is a special case of a more general form obtained from the Hooke's Law:

$$E = \int_{\Gamma} (a + b(H - c_0) + cG)^2 \, \mathrm{d}s, \tag{1.2}$$

where a is the surface tension, b, c are the bending rigidities and c_0 is the spontaneous curvature that describes the asymmetry effect of the membrane or its environment. G is the Gaussian curvature. For simplicity, here we choose to consider only the energy given in (1.1) and we let k be a constant.

The Euler–Lagrangian equation of (1.1) (without the volume and area constraints) can be shown to be

$$\Delta H + 2H(H^2 - G) = 0. \tag{1.3}$$

Notice the above variational problem is closely related to the Willmore's problem [3,20,44]. Energies of (1.1) types can also be found in the study of the configurations of smectic-A liquid crystals [13,23], with connection to the Dupin cyclides [21,23].

One classical method to study the moving interfaces is to employ a mesh that has grid points on the interfaces, and deforms according to the motion of the boundary, such as the boundary integral and boundary element methods (cf. [12,22,42] and their references). Keeping track of the moving mesh may entail computational difficulties and large displacement in internal domains may cause mesh entanglement. Typically, sophisticated remeshing schemes have to be used in these cases.

As an alternative, fixed-grid methods that *regularize* the interface have been highly successful in treating deforming interfaces. These include the volume-of-fluid (VOF) method [24,25], the front-tracking method [18,19] and the level-set method [8,34,35]. Instead of formulating the flow of two domains separated by an interface, these methods represent the interfacial tension as a body-force or bulk-stress spreading over a narrow region covering the interface. Then a single set of governing equations can be written over the entire domain, and solved on a fixed grid in a purely Eulerian framework.

The energetic phase field model can be viewed as a physically motivated level-set method. Instead of choosing an artificial smoothing function for the interface, the diffuse-interface model describes the interface by a mixing energy. This idea can be traced to van der Waals [43], and is the foundation for the phase-field theory for phase transition and critical phenomena (see [5,6,15,31,33,41] and the references therein). The phase field models allow topological changes of the interface [30] and over the years, they have attracted a lot of interests in the field of nonlinear analysis (cf. [1,4,9,37,40]). Similar to the popular level set formulations (see [35] for an extensive discussion), they have many advantages in numerical simulations of the interfacial motion (cf. [8]). When the transition width approaches zero, the phase field model with diffuse-interface becomes identical to a sharp-interface level-set formulation and it can also be reduced properly to the classical sharp-interface model.

In [28,29], we employed numerical methods to simulate the interaction of the flow field with the free vesicles where the surface energy consists only the surface area (which gives rise to the surface tension in the momentum equations). The simulation procedure follows an energetic variational approach. The main attraction for us to use this phase field method is its capability of easily incorporating the complex rheology of microstructured fluids. This is by virtue of its energy-based variational formalism. The conformation of the microstructure is governed by a free energy. This can be added to the mixing energy to form the total free energy of the multi-phase system. Thus, interfacial dynamics and complex rheology are included in a

unified theoretical framework. Our first step in generalizing such a method for the vesicles with bending energy is to formulate the energy given by (1.1) in the phase field framework, which is one of the main contributions of this paper.

Another contribution of this paper is on the numerical solution of the resulting phase field model. While we follow standard approaches to discretize the underlying variational problem with constraints, we take extreme caution in ensuring the convergence of the numerical solutions and conduct extensive simulations in order to probe the energy landscape. Based on the numerical results, we are able to identify many possible solution branches. Some of the configurations, to our knowledge, are obtained for the first time using the numerical simulations. An energy diagram characterizing the solution bifurcation and the hysteresis phenomena is also presented. Such bifurcation studies have not been done systematically in the literature before (cf. [39]). The simulations presented in this paper are only performed for the z-axial symmetric configurations with the prescribed surface area and bulk volume. The axis symmetry limits the number of possible configurations but the rich solution structures can still be illustrated and the computation is reduced to a two-dimensional domain. Full three-dimensional problems without the axis symmetry will be studied in the future.

Many of the configurations, particularly those of discocyte and stomatocyte types, were observed in the experiments as well as other numerical simulations [26]. Due to the nature of our phase field approach and that we did not incorporate the mechanism that can prevent the membrane from splitting, our results include those with nucleation of interior bubbles and holes. On the other hand, this also demonstrate the capability of the phase field approach of going pass the singularities. The problem involving different membrane elasticity properties is under investigation.

The rest of the paper is organized as follows. In Section 2, we develop the framework of the phase field methods and present some brief justifications. In Section 3, we outline the numerical algorithms used to solve the phase field model and provide some numerical tests on the convergence. In Section 4, we present the energy diagram for the solution branches and discuss in detail the various solution branches and their corresponding geometric configurations. In Section 5, we make some concluding remarks. Finally, some details on the discretization schemes are given in Appendix A.

2. Energetic phase field method

We start by introducing a phase function $\phi(x)$, defined on the physical (computational) domain Ω, which is used to label the inside and the outside of the vesicle Γ. We visualize that the level set $\{x : \phi(x) = 0\}$ gives the membrane, while $\{x : \phi(x) > 0\}$ represents the inside of the membrane and $\{x : \phi(x) \leqslant 0\}$ the outside. Define the following modified elastic energy:

$$W(\phi) = \int_{\Omega} \frac{k\epsilon}{2} \left| \Delta\phi - \frac{1}{\epsilon^2}(\phi^2 - 1)\phi \right|^2 \mathrm{d}x, \tag{2.1}$$

where ϵ is a *transition* parameter that is taken to be very small.

If the membrane Γ, which is a surface in Ω, is regular enough, we can always define the following transformation:

$$\phi(x) = q^{\epsilon}\left(\frac{d(x)}{\epsilon}\right), \tag{2.2}$$

where $d(x)$ is the distance of the point $x \in \Omega$ to the surface Γ. Substituting this into (2.1), we have that

$$W(\phi) = \int_\Omega \frac{k}{2\epsilon} \left| q^{\epsilon'} \left(\frac{d(x)}{\epsilon} \right) \Delta d(x) + \frac{1}{\epsilon} \left(q^{\epsilon''} - \left(q^{\epsilon^2} - 1 \right) q^{\epsilon} \right) \right|^2 \mathrm{d}x. \tag{2.3}$$

As $\epsilon \to 0$, in order to minimize the energy, it follows that

$$\left| q^{\epsilon''} - (q^{\epsilon 2} - 1) q^{\epsilon} \right|^2 \to 0 \tag{2.4}$$

which means that $q^\epsilon(\cdot)$ is approaching to the function $\tanh(\cdot/\sqrt{2})$. In the meantime, we see that ϕ is approaching to the Heaviside function with 1 inside of the interface and -1 outside. Γ still coincides with the zero level set of ϕ. Moreover (2.2) indicates that the parameter ϵ is effectively the thickness of the transition region between $\{\phi = 1\}$ and $\{\phi = -1\}$.

In the limit, the energy $W(\phi)$ is approaching to the same energy as in (1.1) (up to a constant multiple). Moreover, the following functional:

$$A = \int_\Omega \phi(x)\, \mathrm{d}x \tag{2.5}$$

goes to the difference of inside volume and outside volume and

$$B = \int_\Omega \left[\frac{\epsilon}{2} |\nabla \phi|^2 + \frac{1}{4\epsilon} (\phi^2 - 1)^2 \right] \mathrm{d}x \tag{2.6}$$

is approaching to $2\sqrt{2}\mathrm{area}(\Gamma)/3$, or about 0.94 times the area of Γ.

Hence we see that the original problem of minimizing the bending energy with the prescribed surface area and bulk volume constraints can be formulated as finding the function $\phi = \phi(x)$ on the whole domain that minimizes the energy $W = W(\phi)$ with the constraints of prescribed values for A and B.

When the energy functional involve more anisotropy terms, we can still apply such an approaches, such as those related in [16,31] with variable rigidity constants.

The advantage of the phase field formulation is that we do not need to track the free surface Γ. The computational domain can remain the same although for computational efficiency, it is natural to select a domain as small as possible so long it properly encloses a suitable neighbor of the membrane under consideration.

3. Numerical simulations

As stated in the prior sections, our problem is to minimize the elastic energy $W(\phi)$ for fixed surface area $3\sqrt{2}B(\phi)/4$ (taking value β) and volume $(A(\phi) + \mathrm{vol}(\Omega))/2$ (taking value α).

This constrained variational problem may be solved by a number of approaches such as the Lagrange Multiplier Method or the method of normalized gradient flow [2]. Here, we adopt the penalty method with penalty coefficients M_1 and M_2. The problem is then becoming the minimization of

$$E(\phi) = W(\phi) + M_1(1/2(A(\phi) + \mathrm{vol}(\Omega)) - \alpha)^2 + M_2(3\sqrt{2}/4B(\phi) - \beta)^2. \tag{3.1}$$

It is easy to argue that minimizers of the above energy (3.1) exist. Moreover, as the penalty constants M_1, M_2 approach to infinity, they approach to the minimizer of $W = W(\phi)$ with the given constraints.

The nonlinear variational problem is solved via a standard gradient flow approach (see for example [2,14] and the references cited therein), namely, we consider

$$\frac{\partial u}{\partial t} = -\frac{\delta E(u)}{\delta u},$$

where $\delta/\delta u$ denote the first variation of the functional. For simplicity, we also use the notation $\nabla E(u)$ to denote this first variation. Given an initial guess, as $t \to \infty$, the dynamic solutions $\{u(t)\}$ converge to a steady state which is a critical point of the energy E [27].

Since we are primarily interested in the minimizers of the energy, only the long time limit of the above gradient flow is important. A backward Euler scheme is employed for the time integration of the above gradient flow to ensure the stability of the time integration and to allow large time steps to be taken for a faster convergence to the steady state. That is

$$u^{n+1} - u^n = -\Delta t_n \frac{\delta E(u^{n+1})}{\delta u} = -\Delta t^n \nabla E(u^{n+1}).$$

As in [2,14], it is easy to verify that the solution of the backward Euler scheme is also the solution of the minimization problem

$$\min \tilde{E}^n(u) = \int_\Omega \frac{|u - u^n|^2}{\Delta t_n}\, \mathrm{d}x + E(u). \tag{3.2}$$

Since

$$E(u^{n+1}) \leqslant \tilde{E}^n(u^{n+1}) \leqslant \tilde{E}^n(u^n) = E(u^n),$$

we see that the backward Euler scheme enjoys the property that the energy is monotonically decreasing in time. Moreover, $u^n \to \phi$, a critical point of the energy E, as $n \to \infty$.

To implement the gradient flow approach, a spatial approximation is first established. As the numerical simulations presented in this paper concern mainly on the z-axial symmetrical cases, the three-dimensional problem is thus simplified to a two-dimensional one. The computational domain is taken to be a subset of the half plane in the x–z plane. The cross-section of the vesicle in this half plane ($x > 0$) is computed and the vesicle is obtained by rotating the two-dimensional shape on the x–z plane around the z-axis. Thus effectively, we may relate x with the radial distance to the z-axis. Without loss of generality, we let the cross-section of the vesicle be located inside the domain $[0, r] \times [0, a]$ on the x–z plane. The energy functional 3.2 is then discretized on a spatial $m \times n$ mesh in the domain $[0, r] \times [0, a]$ in the x-z plane using standard difference approximations, which leads to a discrete gradient flow. The particular form of the discretization is given in Appendix A.

We note that, in our computation domain, the cross-section of the vesicle surface Γ of interest becomes a one-dimensional curve, which can be parameterized by a single variable. Though a reduction to an ordinary differential–integral equation is possible, such a formulation generally works well only when the curve does not undergo any topological changes. The phase field approach developed here can handle such changes with ease and it can be used for the full three-dimensional computation as well, including the anisotropic cases.

The solution of the Euler scheme for the discrete gradient flow at each step satisfies a nonlinear system of equations and it is solved by the Newton's method. The resulting systems of linear equations at each Newton iteration are solved using a version of the PCG method for sparse matrices with an ICC preconditioner. Newton's method is generally locally convergent. For a small enough time step, the new solution is very close to the solution at the previous time step, and the Newton's iteration converges quickly to a critical point of $\tilde{E}$. However, small Δt_n implies that many time integration steps have to be taken in order to converge to the steady state. In our algorithm, we adjust the value of Δt_n so that the Newton's method always converges in 3–5 steps. This allows efficient computation at each time step. At the same time, it leaves room for a large step size when the solution is not varying very fast in time, and thus leads to a speedy convergence to the steady state. We leave detailed descriptions of the algorithm in Appendix A.

For a particular phase field simulation, the quality of the numerical result is affected by the choice of computational domain, the transition thickness parameter (or the effective width of the diffusive interface) ϵ, the number of grid points, and the choices of other parameters used in the simulation. Based on the experience, we generally take a domain significantly larger than the region enclosed by the membrane to be computed. The parameter ϵ is taken to be just a couple of percentage points of the domain size to ensure a relatively sharp interfacial region. The mesh size is normally taken to be several times smaller than ϵ to ensure adequate spatial resolution. To ascertain the accuracy and robustness of our numerical algorithms and the parameter selections, we here present results of some numerical tests on the convergence and performance of our method.

The first example is for the same set of parameters (ϵ, α and β) in the same domain of size 2 by 2, but with different grids of the size 100×100 and 200×200, respectively. We choose $\epsilon = 0.03$, volume $\alpha = 1.1000$ and the area $\beta = 6.9474$ and the penalty parameters $M_1 = M_2 = 10^5$.

The density plots of two numerical approximations of ϕ are shown in Fig. 1. Little difference between the solutions is visible. Moreover, the computation of the energy W gives energy valued at 71.8767 and 73.4440, respectively. The 2% energy difference is mostly due to the integration errors under different grids.

The convergence is also evident when different domain sizes are used (so long they are large enough to contain the vesicle). We compute the problem using two different grids, a 100×150 grid and a 40×375 grid, but with same mesh parameter ($h = 0.02$). This effectively leads to two different domains of sizes 2×3 and 0.8×7.5 (see the results in Fig. 2). The same parameters as in the previous run (depicted in Fig. 1) are used, except with the area $\beta = 6.3640$. The energy is 60.6037 for the 100×150 grid and 61.2120 for the

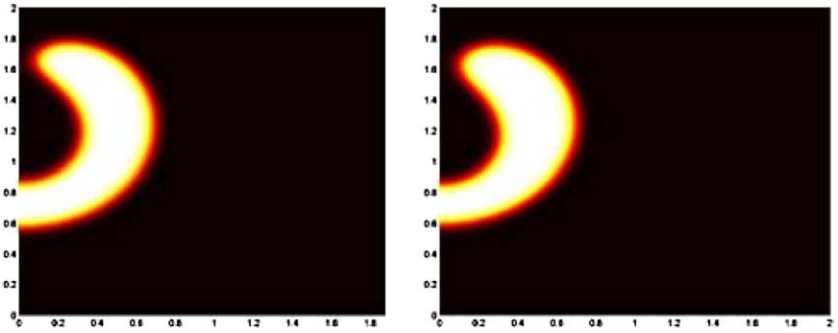

Fig. 1. Density plots of ϕ with 100×100 and 200×200 grids.

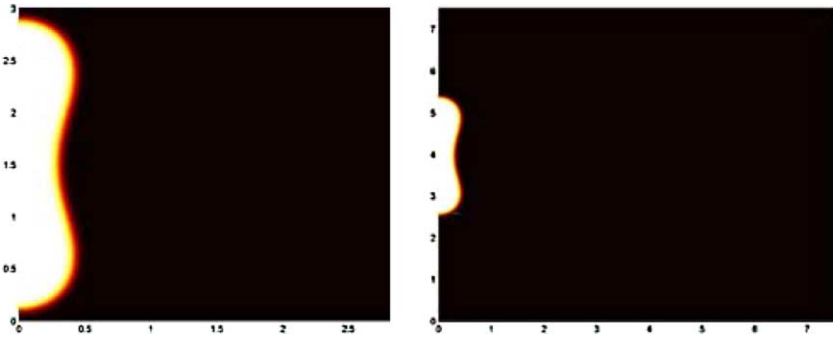

Fig. 2. Computation on different domains using 100×150 and 40×375 grids.

Table 1
Convergence of the multipliers

$M_1 = M_2$	1	2	4	8	16
λ_1 ($\times 10^{-2}$)	4.0428	3.6964	3.5577	3.4951	3.4669
λ_2 ($\times 10^{-3}$)	−1.0198	−0.9224	−0.8832	−0.8655	−0.8576
$M_1 = M_2$	32	64	128	256	512
λ_1 ($\times 10^{-2}$)	3.4526	3.4424	3.4401	3.4372	3.4376
λ_2 ($\times 10^{-3}$)	−0.8535	−0.8506	−0.8495	−0.8491	−0.8492

40×375 grid. The small error indicates that the result is insensitive to the change of the computation domain.

We also investigate the dependence on the penalty parameters M_1 and M_2. For the case of 200×200 grid and the set of parameters being the same as in Fig. 2, we list the values of the corresponding Lagrange multipliers λ_i ($i = 1, 2$) in Table 1. For minimizing the energy W given in (2.3) with constraints $g1 = 0$ and $g2 = 0$ (for area and volume), the multipliers are defined as constants satisfying

$$\lambda_1 \nabla g1 + \lambda_2 \nabla g2 + \nabla W = 0$$

at the minimum. Here, ∇ again refers to first variations of the respective functionals. With the penalty formulation, the relations between the multipliers and the penalty constants are given by

$$\lambda_i = \lim_{M_1, M_2 \to \infty} \lambda_i(M_1, M_2) \quad \text{for } i = 1, 2$$

with $\lambda_1(M_1, M_2) = M_1(A(\phi) + \mathrm{vol}(\Omega) - 2\alpha)$, $\lambda_2(M_1, M_2) = M_2(3\sqrt{2}B(\phi)/2 - 2\beta)$.

We can see that for the ever increasing penalty coefficients M_1, M_2, the multipliers converge to two constants. This confirms that our solutions indeed are the constrained minimizers of the energy functional.

The final example is designed to test the dependence on the parameter ϵ which measures the interface thickness. As it is well known that, the grid size has to be smaller than the thickness of the transition layer in order to resolve the interface, we thus take the 100×200 grid, with $\beta = 5.8867$ and $\alpha = 1.1000$, for ϵ being 0.02 and 0.015. The difference in the numerical solutions is very small, as shown in Fig. 3 and the corresponding energy values 73.6980 and 72.7080 are very close to each other.

To summarize, the above numerical tests indicate that the simulation of the phase field model can indeed give convergence numerical solutions. Moreover, as our above experimental results indicate the choices of various parameter values used in the simulations are capable of ensuring the convergence of the numerical

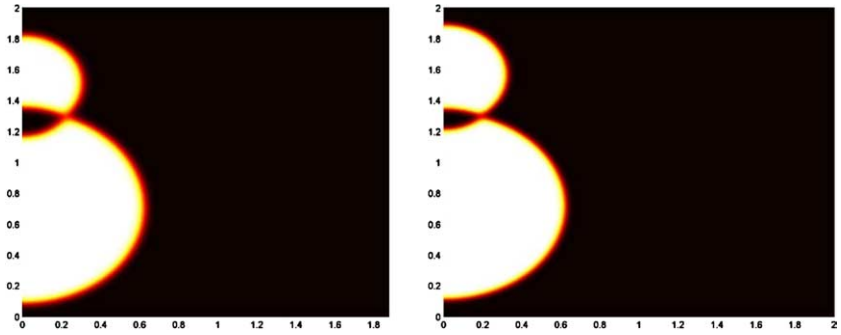

Fig. 3. The computation under different thickness ϵ: 0.02 vs. 0.015.

scheme and ensuring the validity of the simulation results when we probe the energy landscape and predict the vesicle shapes.

4. Simulation results

We now presents computational results that illustrate the various vesicle structures and the energy landscape.

For the numerical simulations, through a re-scaling, we may take a fixed volume value α and vary the surface area β. In all the simulations, we take the volume enclosed by the vesicle to be 1.1000 (the particular value has no physical significance as it is due to a inadvertently chosen scaling in the simulations). For a perfect sphere, it corresponds to the radius being 0.6404 with the surface area being 5.1536.

For different values of the surface area β with a given volume α that is enclosed by the surface, the different basic shapes (density plots of ϕ) obtained in the simulation are shown in Fig. 4. The sharp contrast of the change of color outlines the vesicle boundary. Here, rather than using sophisticated physiological or biological terminologies, we try to use some more common objects to name the various shapes judging from their shape resemblance (viewed in the three-dimensional space). For a better visual effect, we give some three-dimensional views in Fig. 5. Though the shapes computed having the same volume, they have different aspect ratios that make them difficult to be displayed in pictures with the same scale. For this reason, the plots in Figs. 4 and 5 do not share the same scale and the some vesicle shapes may appear larger than others.

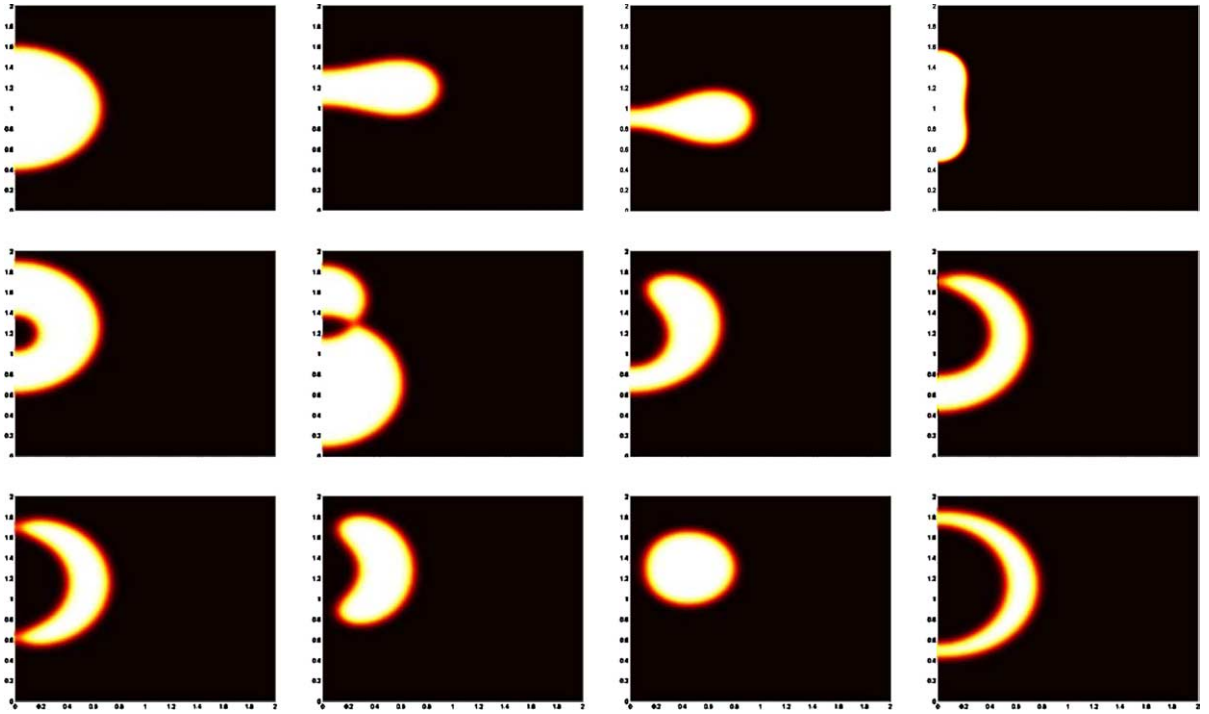

Fig. 4. The basic configurations: ball, pancake, dimpled-disc, gourd, longan, twin-bubble, round-pot, cherry, pitomba, bangle, torus and shell.

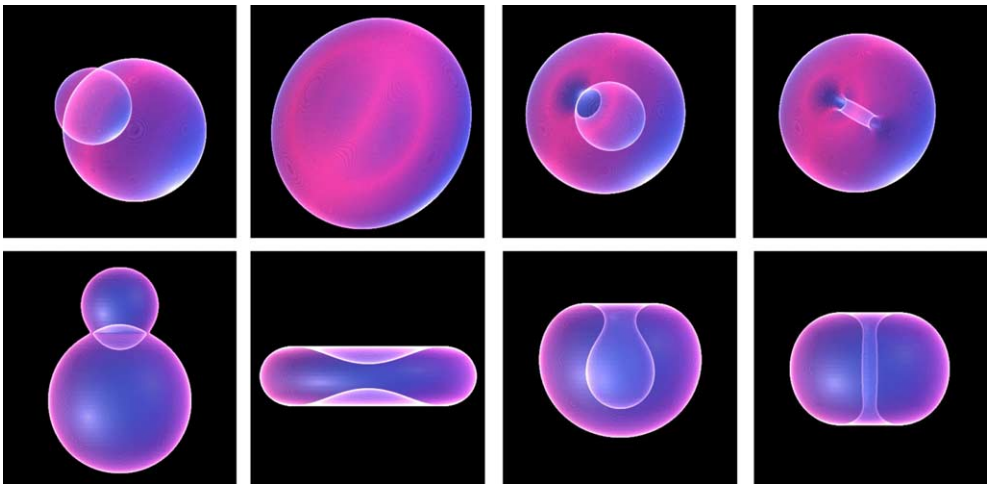

Fig. 5. 3D views of the twin-bubble, dimpled disc, round-pot and torus.

Naturally, some of the shapes in Fig. 4 are very similar to each other and are not necessarily topologically different from each other. In biological terms, the pancake or dimpled-disc shape may be referred as a discocyte while the round-pot, cherry or pitomba shape are classified as a stomatocyte (mouth). These shapes have been experimentally observed. Other non-axisymmetric vesicle shapes exist as well but they are not discussed here.

Fig. 6 shows the overall energy landscape and the hysteresis of the solution branches. The numerical values of the energy in all figures in this paper are those of $W(\phi)$ in (2.3). In the energy plots, the vertical axis corresponds to the energy and the values of the area β are represented by the horizontal axis. The various solution branches are computed through the path following approach. When a particular solution

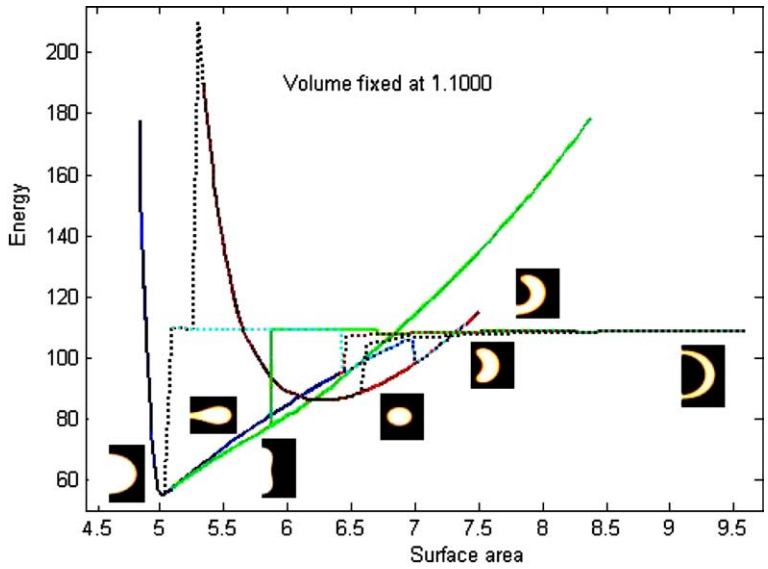

Fig. 6. Global energy landscape and hysteresis loops.

branch loses its stability when we probe the parameter values, the numerical solution may jump to a different branch, we record the values of the parameters at which such jumps take place. As we are solving a nonlinear problem, hysteresis phenomena are expected, that is, when the parameter goes up and down, the solution may follow different paths.

We now give detailed explanation to each of the curves in Fig. 6. The arrows along the curves in the later energy pictures indicate the directions of the change of the area value. The reference to the color scheme may be ignored if monochrome display or printout is used.

We begin by examining the red line redrawn in Fig. 7 (left), which is for the deformation of the torus shape. The curve can be extended infinitely on both ends. The shape is stable, in the sense that if we start from the configuration on the curve, it stays on the curve when the surface area changes. There is also a vertical asymptotic limit at the left end. When the area is less than such a critical value, the shape changes and it becomes the shape of a longan (an outer sphere containing a small spherical core, this name is used to distinguish from the solution branch representing the shell shape). In Fig. 8, we give an example to illustrate the changing of the shape.

The blue line redrawn in Fig. 7 (right) consists of three different deformations. When the area is small (<5.0117), the vesicle shape looks like a ball. However, the surface area in this case is too small to keep up with the volume. In reality, there is simply no solution, i.e., no corresponding geometric shape. In the phase

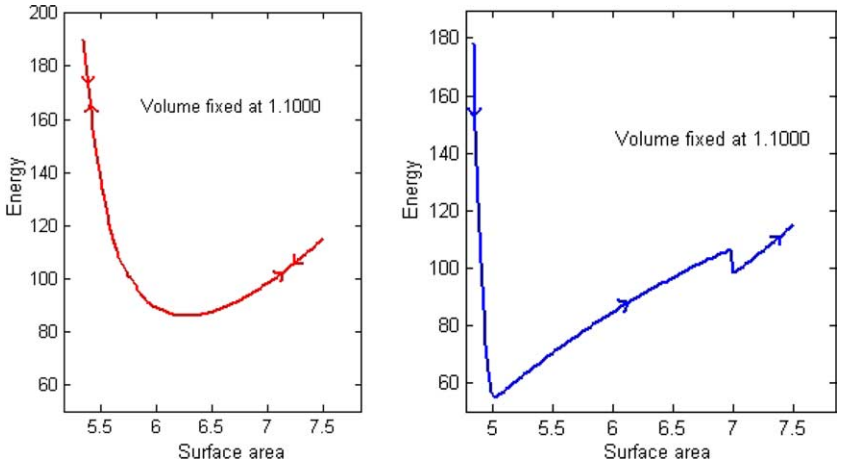

Fig. 7. The change of energy for a torus shape (left) and for a spherical ball to a pancake, a dimpled-disc then to a torus (right).

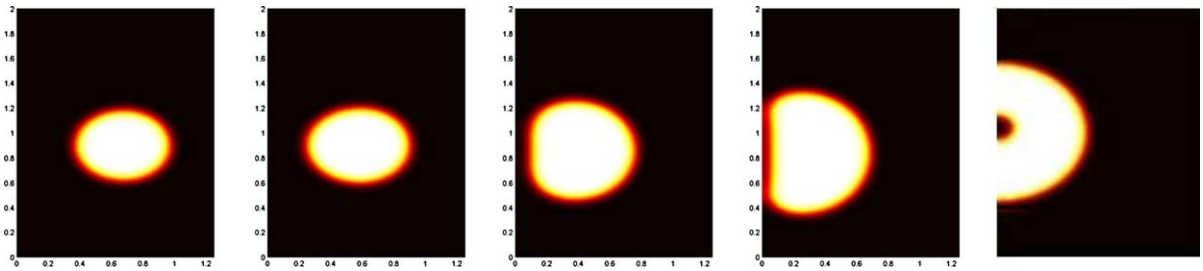

Fig. 8. Deformation of torus with areas at: 7.4246, 6.8943, 5.8336, 5.3457, and 5.1972.

field formulation, the solution exists due to an extension of the interface width. From the value 5.0117 to 6.9792, the vesicle changes the shape from a spherical ball to a pancake. After the value increase to 7.0004, the shape of the vesicle makes a jump to a torus (and the energy actually drops). Fig. 9 shows such a transformation.

The green solid line, redrawn in Fig. 10, is for the deformation of gourd shape. It is stable in both directions (with area either increasing or decreasing) in the sense that small perturbations do not drive the solution onto other branches. This green solid line coincides with the blue dash line, which appears in Fig. 7 (right), below value 5.0117 (when they all become spherical ball), see Fig. 11 for an illustration.

When the area is between 5.0117 and 5.1018, the energy value of the pancake is lower than the gourd. It then surpasses the later after the value 5.1018, see Fig. 12. If we start at a ball and increase the area, it goes

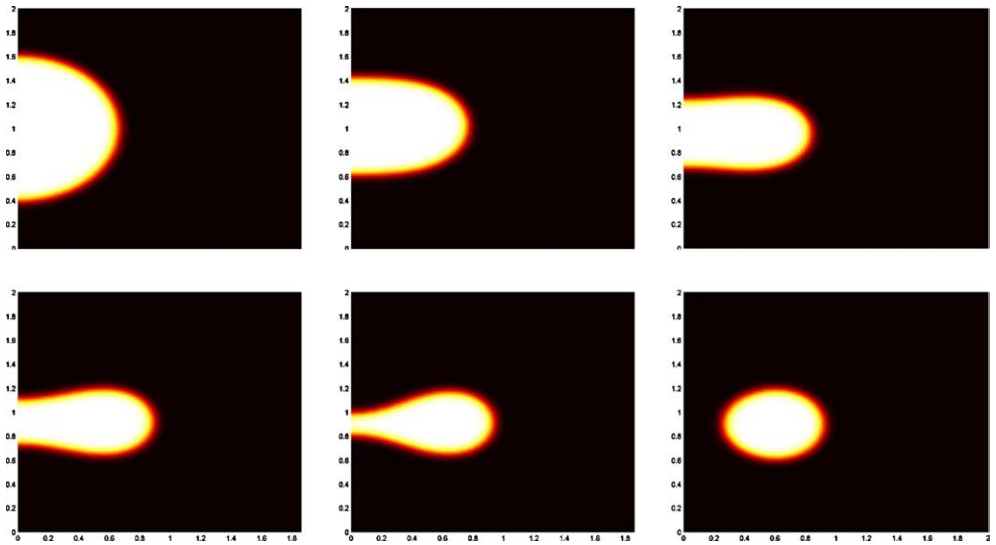

Fig. 9. Deformation of a ball to pancakes, a dimpled-disc and then to a torus with the area valued at: 5.0275, 5.3457, 5.8336, 6.3640, 6.9791 and 7.0004.

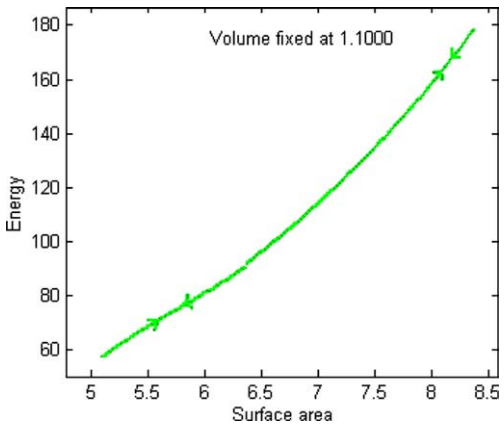

Fig. 10. The change of energy for the gourd shape.

to a pancake and then to a torus when the area becomes large. Both solution curves, however, are stable individually (checked by the numerical simulations with the addition of small perturbations).

The green line in Fig. 13 indicates that the twin-bubble shape in Fig. 4 jumps to the gourd shape when the area decreases. However, this process is not reversible: when the area of a gourd increases (Fig. 14), it keeps on being a gourd as in Fig. 10 (the green line). When the area of a twin-bubble increases, it changes to a round-pot (cherry) shape and then to a shell shape. However, the energy is almost the same (even with possible small jumps) (Fig. 15).

The dotted black line in Fig. 16 indicates the deformation of a shell shape when the area decreases. It first leads to a bangle (with no obvious energy jump), then to a torus (with energy jump at $\beta = 6.6027$), then a longan (energy jump at around $\beta = 5.2768$) and finally to a spherical ball (energy jump at around $\beta = 5.0647$) (Fig. 17). It overlaps with part of the red line in Fig. 7 (left). Corresponding to each piece of the energy curve (in between the jumps), the curve is reversible, that is, the shapes can change back and forth between the jumps.

The dotted cyan curve in Fig. 18 indicates the change of the shape of longan to a pancake (or a discocyte, a dimpled-disc), and then a torus when the area increases, as in Fig. 19 illustrated. The energy shows (small) jumps whenever there is a topological change of the configuration.

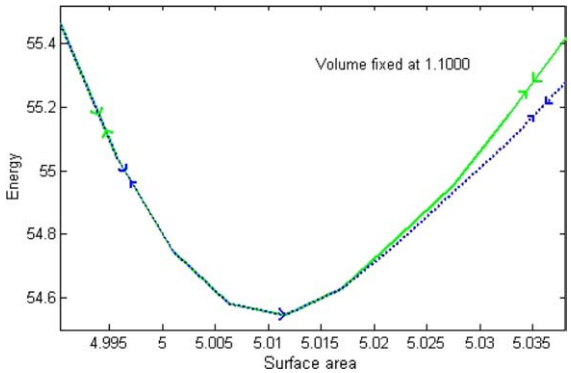

Fig. 11. Both the pancake and the gourd shrink to the same ball when the area is small.

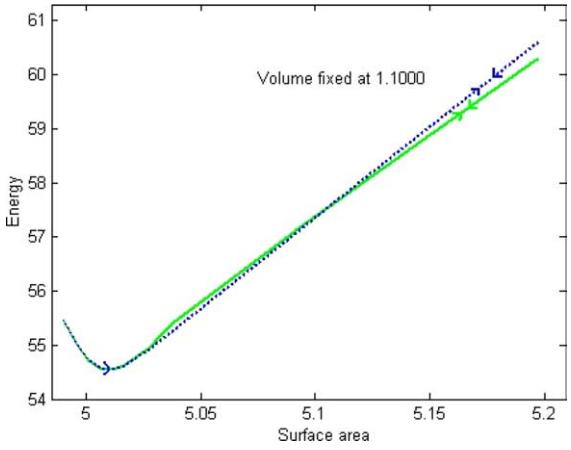

Fig. 12. The energy of the pancake surpasses that of the gourd.

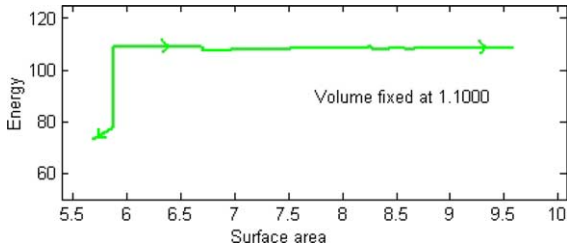

Fig. 13. The change of energy for a twin-bubble to a gourd and a shell.

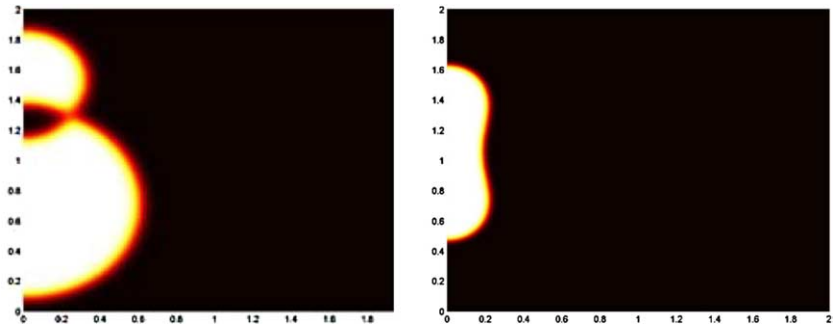

Fig. 14. The deformation of a twin-bubble to a gourd with areas 5.8867 and 5.8761.

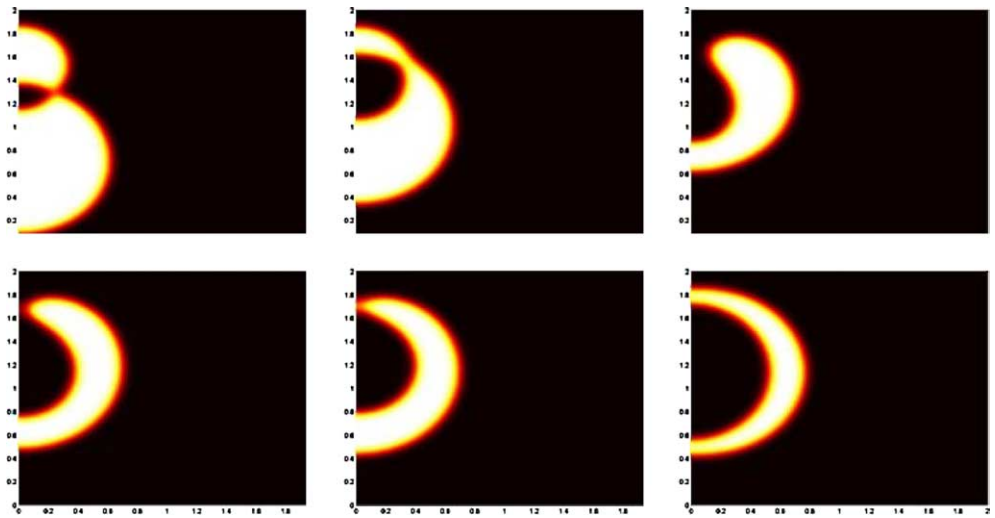

Fig. 15. The deformation of a twin-bubble to a round-pot and then a shell with a fixed volume and areas of: 5.8867, 6.6928, 6.7140, 7.7322, 7.9656 and 10.6278.

Finally, the dotted red curve in Fig. 20 indicates the change of the shape of cherry to a round-pot then to a pancake when the area increases, as in Fig. 21 illustrated. The jump to the pancake shape occurs at the same value of surface area as the jump from the longan shape to the pancake depicted in Fig. 19. Before the jump, the energy stays very close to that of the black dotted line in Fig. 16 and is only slightly larger. One

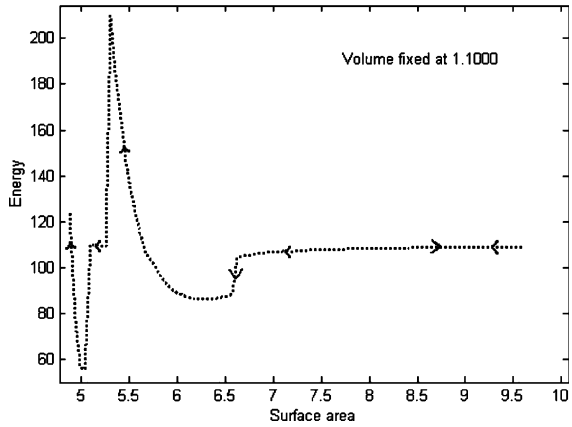

Fig. 16. Deformation of a shell shape with decreasing area.

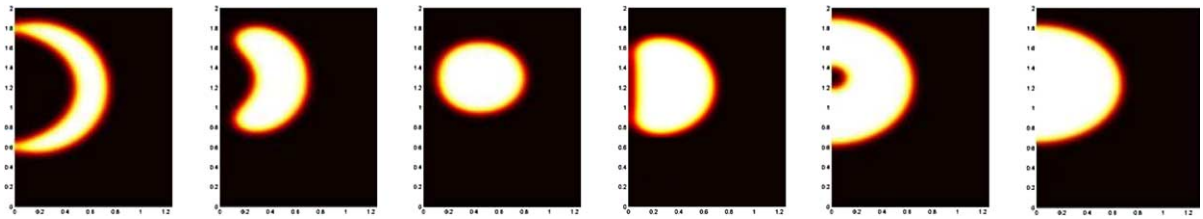

Fig. 17. Deformation of a shell to a bangle, a torus, a longan and finally a ball with the area valued at: 9.5459, 6.6291, 6.0988, 5.3457, 5.1972 and 5.0381.

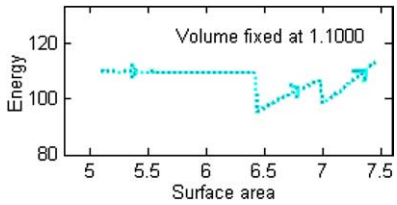

Fig. 18. The change of energy from longan to a pancake, and a torus.

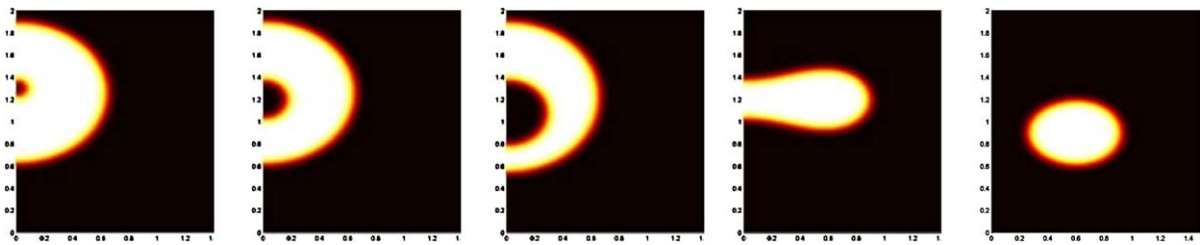

Fig. 19. The deformation of a longan to a pancake and then to a torus when the volume fixed and the area valued at: 5.0912, 5.4624, 6.4170, 6.4435 and 7.0004.

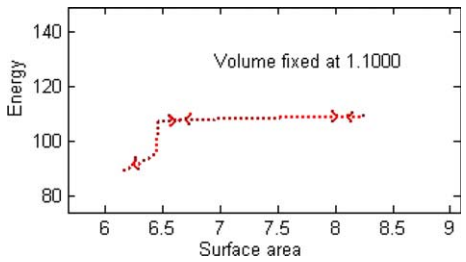

Fig. 20. The change of energy from a cherry to a round-pot, then a pancake.

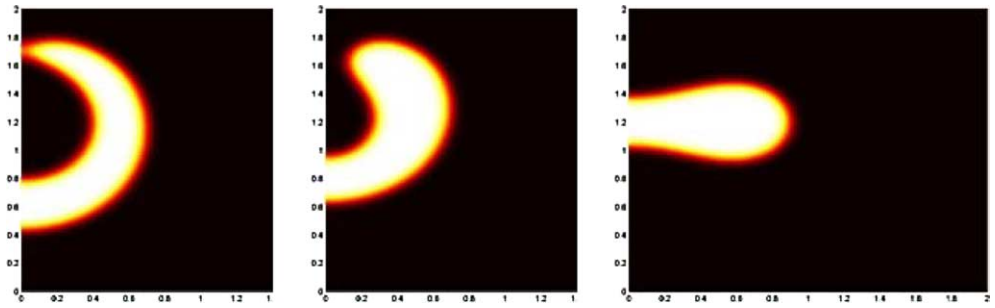

Fig. 21. The deformation of a cherry to a round-pot and then a jump to a pancake when the volume fixed and the area valued at: 7.9656, 6.4594, 6.4382.

may view the two close solution branches as one with the symmetry (in the z variable) and one that loses the symmetry.

Based on the above results, we see that the application of the phase field approach to the computation of z-axial symmetric vesicle leads to various interesting configurations that of different shapes. In Fig. 22, we summarize the transformations between the different shapes, the arrows point to directions with increasing areas along the solution paths. Some of the configurations, to our knowledge, are obtained for the first time using the numerical simulation.

Clearly, due to the z-axial symmetry imposed on the solutions, we may not be able to reach from one particular configurations to all other configurations with the continuation in the area parameter. Further investigation with full three-dimensional simulations is needed in order to give a complete description of the

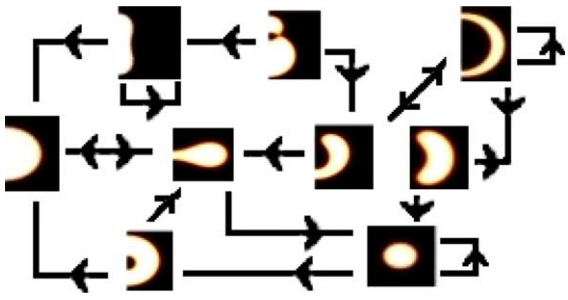

Fig. 22. A pictorial illustration of solution paths through various configurations.

solution manifold. Nevertheless, the simulation results presented here again demonstrate the effectiveness of the phase field approach in tracking surfaces of varying topologies.

5. Conclusion

In this paper, we study the static deformation of a vesicle membrane under the elastic bending energy, with prescribed bulk volume and surface area. We discover several axial symmetric configurations using numerical simulations. The energetic bifurcation landscape is also examined. The application of the phase field formulation gives us the advantage of avoiding keeping track the free interfaces. Moreover, this approach fits in existing methods developed to study the interaction of these configurations and the external applied fields, the specific species inside and surrounding the vesicle, and other surface energies (due to anisotropy). More extensive three-dimensional simulations and more detailed analysis will be carried out in our future works.

Acknowledgements

The authors thank the referees for their valuable suggestions that have improved the presentation of our paper.

Appendix A. Discretization and algorithms

Here, we provide more detailed descriptions of the discrete energy and the numerical algorithm.

We use a uniform $m \times n$ mesh with h being the mesh parameter so that $r = mh$, and $a = nh$. The differential operators is replaced by the standard finite difference operators defined on the given mesh.

Discrete energy. Recall that the energy functional has the form

$$E = \int_\Omega \frac{k\epsilon}{2}\left|\Delta\phi - \frac{1}{\epsilon^2}(\phi^2-1)\phi\right|^2 \mathrm{d}x + M_1\left(\int_\Omega \phi(x)\,\mathrm{d}x - \alpha\right)^2 + M_2\left(\int_\Omega \left[\frac{\epsilon}{2}|\nabla\phi|^2 + \frac{1}{4\epsilon}(\phi^2-1)^2\right]\mathrm{d}x - \beta\right)^2. \tag{A.1}$$

To discretize the energy functional (A.1), we use the following quadrature:

$$\int_\Omega f(\mathbf{x})\,\mathrm{d}\mathbf{x} \approx I_h(f) = \frac{2}{9}\pi h^3 \sum_{i=1}^{m}\sum_{j=0}^{n} \mathrm{i}\omega_1(i)\omega_2(j) f_{i,j} \tag{A.2}$$

for any function f defined on Ω, where $f_{i,j}$ is the value of f at the grid point (ih, jh) in the $m \times n$ mesh, and weight functions ω_1 and ω_2 are defined as following:

$$\omega_1(i) = \begin{cases} 1 & \text{if } i = 0 \text{ or } m, \\ 2 & \text{if } i \text{ is even and } i \neq m, \\ 4 & \text{otherwise} \end{cases} \tag{A.3}$$

and

$$\omega_2(j) = \begin{cases} 1 & \text{if } j = 0 \text{ or } n, \\ 2 & \text{if } j \text{ is even and } i \neq n, \\ 4 & \text{otherwise.} \end{cases} \tag{A.4}$$

Now, let us turn to the discretization of the terms $\Delta\phi$ and $|\nabla\phi|^2$. Since

$$\Delta\phi(r,z) = \frac{\partial^2\phi}{\partial r^2} + \frac{\partial^2\phi}{\partial z^2} + \frac{1}{r}\frac{\partial\phi}{\partial r} \quad \text{and} \quad |\nabla\phi(r,z)|^2 = \left(\frac{\partial\phi}{\partial r}\right)^2 + \left(\frac{\partial\phi}{\partial z}\right)^2, \tag{A.5}$$

we take their discrete forms as follows:

$$(\Delta_h\phi)_{i,j} = \frac{\phi_{i,j+1} + \phi_{i,j-1} + \phi_{i+1,j} + \phi_{i-1,j} - 4\phi_{i,j}}{h^2} + \frac{\phi_{i+1,j} - \phi_{i-1,j}}{2ih^2}, \tag{A.6}$$

$$|(\nabla_h\phi)_{i,j}|^2 = \frac{(\phi_{i,j+1} - \phi_{i,j-1})^2 + (\phi_{i+1,j} - \phi_{i-1,j})^2}{4h^2}. \tag{A.7}$$

The discrete boundary conditions are $\phi_{m+1,i} = -1$ and $\phi_{j,-1} = \phi_{j,n+1} = -1$ for $i = 0, 1, \ldots, m$ and $j = 0, 1, \ldots, n$. Here, we also set $\phi_{0,j} = \phi_{1,j}$ for all j at the z-axis. The boundary conditions are applied to the formula (A.6) and (A.7) at the boundary. In our numerical simulation, as a comparison, we also implemented a cell centered difference approach in the x (or r) direction, that is, the grid points in x are at the points $\{(i+1/2)h\}_{i=0}^{n-1}$. We then introduce a ghost point at $-h/2$ and impose the boundary condition $\phi(-h/2, z_j) = \phi(h/2, z_j)$ for all j. In such a discretization, grids points avoid the z-axis. Numerical experiments indicate that the two discretization approaches yield effectively the same results.

Combine (A.1), (A.2), (A.6) and (A.7), we can get the discrete form of the energy, which we denote by E_h. The existence of minimizers for E_h is easy to establish for any given mesh. The convergence of the discrete minimizers to minimizers of the continuous problem can also be established as the mesh parameters goes to zero, at least for any fixed parameter ϵ. The limiting behavior for small ϵ and small mesh parameter h is a delicate issue that will be studied more carefully in our future works. For convenience, we let ∇E_h denote the gradient vector of E_h and $\triangle E_h$ denote the Hessian matrix of E_h.

Gradient flow algorithm. Clearly, a critical point of the energy E_h corresponds to a grid function at which all components of ∇E_h vanish. For a more efficient implementation, we adopt a strategy to dynamically constrain some values of the grid function during the solution process. In particular, at grid points that correspond to small gradient components, changes of the grid function make insignificant contribution to the variation in energy, thus, no update of the grid function values at those grid points is performed. As the grids points correspond to large gradient components often are located near the interface, such a strategy naturally leads to a fast algorithm that allow the computation being more focused in the vicinity of the phase boundary (in the same spirit of the fast level set methods [35]). The details are given in the following.

Given α, β, ε, and penalty parameters M_1, M_2.

1. Initialize $\mathbf{u}_{\text{old}} = \mathbf{u}_0$ to match with an initial shape and take an initial small time step Δt.
2. Compute $\nabla E_h(\mathbf{u}_0)$, put constraints on the components $\{u_i\}$ of $\mathbf{u}_0$ that correspond to grid points with small $\{\partial E_h/\partial u_i\}$ and their adjacent points.
3. Compute using Newton's method to get a new solution $\mathbf{u}_1 = \mathbf{u}_0 - (\Delta E(\mathbf{u}_0) + 2I/(\Delta t))^{-1}(\nabla E_h(\mathbf{u}_0) + 2(\mathbf{u}_0 - \mathbf{u}_{\text{old}})/(\Delta t))$ where the updates only take place for unconstrained components.
4. Continue Newton's iteration with

$$\mathbf{u}_{k+1} = \mathbf{u}_k - (\Delta E(\mathbf{u}_k) + 2I/(\Delta t))^{-1}(\nabla E_h(\mathbf{u}_k) + 2(\mathbf{u}_k - \mathbf{u}_{\text{old}})/(\Delta t))$$

   for unconstrained components and for $k = 1, 2, \ldots$ until the norm $\|\nabla E_h(\mathbf{u}_k) + 2(\mathbf{u}_k - \mathbf{u}_{\text{old}})/(\Delta t)\|$ is smaller than some given tolerance. Denote the solution as $\mathbf{u}_{\text{new}}$. If the number of Newton steps in this loop is larger than 5, stop.
5. If the number of iteration in step 4 is larger than 5, half Δt, return to step 3 to repeat Newton's method; If the iteration number is less than 3, double Δt.

6. Compute $\|\nabla E(\mathbf{u}_{\text{new}})\|$, if small enough, exit. Otherwise set $\mathbf{u}_{\text{old}} = \mathbf{u}_0 = \mathbf{u}_{\text{new}}$ and go to step 2.

As noted before, the linear systems in steps 3 and 4 are solved using the PCG method for sparse matrices with an ICC preconditioner. Our numerical experiments indicate that the above algorithm is very stable and robust.

References

[1] N.D. Alikakos, P.W. Bates, X.F. Chen, Convergence of the Cahn–Hilliard equation to the Hele–Shaw model, Arch. Rational Mech. Anal. 128 (1994) 165–205.

[2] W. Bao, Q. Du, Computing the ground state of the BEC via normalized gradient flow, 2003 (preprint). Available from <http://arxiv.org/abs/cond-mat/0303241>.

[3] R.L. Bryant, Surfaces in conformal geometry, in: The Mathematical Heritage of Hermann Weyl (Durham, NC, 1987), Proc. Sympos. Pure Math., vol. 48, American Mathematical Society, Providence, RI, 1988, pp. 227–240.

[4] G. Caginalp, X.F. Chen, Phase field equations in the singular limit of sharp interface problems, in: On the Evolution of Phase Boundaries (Minneapolis, MN, 1990–91), Springer, New York, 1992, pp. 1–27.

[5] J.W. Cahn, S.M. Allen, A microscopic theory for domain wall motion and its experimental verification in fe–al alloy domain growth kinetics, J. Phys. Colloque C7 (19778) C7–51.

[6] J.W. Cahn, J.E. Hillard, Free energy of a nonuniform system. I. Interfacial free energy, J. Chem. Phys. 28 (1958) 258–267.

[7] R.S. Chadwick, Axisymmetric indentation of a thin incompressible elastic layer, SIAM J. Appl. Math. 62 (2002) 1520–1530.

[8] Y.C. Chang, T.Y. Hou, B. Merriman, S. Osher, A level set formulation of Eulerian interface capturing methods for incompressible fluid flows, J. Comput. Phys. 124 (1996) 449–464.

[9] X.F. Chen, Generation and propagation of interfaces in reaction–diffusion systems, Trans. Am. Math. Soc. 334 (1992).

[10] P.G. Ciarlet, Introduction to Linear Shell Theory, Series in Applied Mathematics (Paris), vol. 1, Gauthier-Villars, Éditions Scientifiques et Médicales Elsevier, Paris, 1998.

[11] P.G. Ciarlet, Mathematical elasticity, vol. III, in: Studies in Mathematics and its Applications, vol. 29, North-Holland, Amsterdam, 2000, Theory of shells.

[12] V. Cristini, J. Blawzdziewicz, M. Loewenberg, Drop breakup in three-dimensional viscous flows, Phys. Fluids 10 (1998) 1781–1783.

[13] P.G. de Gennes, The Physics of Liquid Crystals, Oxford University Press, Oxford, 1974.

[14] Q. Du, Finite element methods for the time dependent Ginzburg–Landau model of superconductivity, Comput. Math. Appl. 27 (1994) 119–133.

[15] J.E. Dunn, J. Serrin, On the thermomechanics of interstitial working, Arch. Rational Mech. Anal. 88 (1985) 95–133.

[16] C.M. Elliott, R. Schätzle, The limit of the fully anisotropic double-obstacle Allen–Cahn equation in the nonsmooth case, SIAM J. Math. Anal. 28 (1997) 274–303.

[17] Y.C. Fung, Biomechanics: Mechanical Properties of Living Tissues, Springer, New York, 1981.

[18] J. Glimm, X.L. Li, Y. Liu, N. Zhao, Conservative front tracking and level set algorithms, Proc. Natl. Acad. Sci. USA 98 (2001) 14198–14201.

[19] J. Glimm, J.W. Grove, X.L. Li, D.C. Tan, Robust computational algorithms for dynamic interface tracking in three dimensions, SIAM J. Sci. Comput. 21 (2000) 2240–2256.

[20] F. Hélein, A Weierstrass representation for Willmore surfaces, in: Harmonic Morphisms, Harmonic Maps, and Related Topics (Brest, 1997), Chapman & Hall/CRC Res. Notes Math., vol. 413, Chapman & Hall/CRC, Boca Raton, FL, 2000, pp. 287–302.

[21] D. Hilbert, S. Cohn-Vossen, Geometry and the Imagination, Chelsea Publishing Company, New York, NY, 1952 (Transl.: P. Neményi).

[22] R.E. Khayat, Three-dimensional boundary-element analysis of drop deformation for Newtonian and viscoelastic systems, Int. J. Numer. Meth. Fluids 34 (2000) 241–275.

[23] D. Kinderlehrer, C. Liu, Revisiting the focal conic structure in smectic-A, in: R. Batra, M.F. Beatty (Eds.), Contemporary Research in the Mechanics and Mathematics of Materials, CIMNE, 1998.

[24] J. Li, Y. Renardy, Numerical study of flows of two immiscible liquids at low Reynolds number, SIAM Rev. 42 (2000) 417–439.

[25] J. Li, Y. Renardy, Shear-induced rupturing of a viscous drop in a Bingham liquid, J. Non-Newtonian Fluid Mech. 95 (2000) 235–251.

[26] G. Lim, M. Wortis, A numerical study of the mechanics of red blood cell shapes and shape transformations. Available from <http://www.sfu.ca/ghlim/presentation/title.html>.

[27] F.-H. Lin, Q. Du, Ginzburg–Landau vortices, dynamics, pinning and hysteresis, SIAM J. Math. Anal. 28 (1999) 1265–1293.

[28] C. Liu, J. Shen, A phase field model for the mixture of two incompressible fluids and its approximation by a Fourier-spectral method, Physica D 179 (2003) 211–228.

[29] C. Liu, N.J. Walkington, An Eulerian description of fluids containing visco-hyperelastic particles, Arch. Rat. Mech. Anal. 159 (2001) 229–252.
[30] J. Lowengrub, L. Truskinovsky, Quasi-incompressible Cahn–Hilliard fluids and topological transitions, R. Soc. Lond. Proc. Ser. A 454 (1998) 2617–2654.
[31] G.B. McFadden, A.A. Wheeler, R.J. Braun, S.R. Coriell, R.F. Sekerka, Phase-field models for anisotropic interfaces, Phys. Rev. E 48 (3) (1993) 2016–2024.
[32] L. Miao, U. Seifert, M. Wortis, H. Dobereiner, Budding transitions of fluid-bilayer vesicle: the effect of area-difference elasticity, Phys. Rev. E 49 (1994) 5389–5407.
[33] W.W. Mullins, R.F. Sekerka, On the thermodynamics of crystalline solids, J. Chem. Phys. 82 (1985).
[34] S. Osher, J. Sethian, Fronts propagating with curvature dependent speed: algorithms based on Hamilton Jacobi formulations, J. Comput. Phys. 79 (1988) 12–49.
[35] S. Osher, R. Fedkiw, The Level Set Method and Dynamic Implicit Surfaces, Springer, Berlin, 2002.
[36] Z. Ou-Yabg, W. Helfrich, Bending energy of vesicle membranes: general expressions for the first, second and third variation of the shape energy and applications to spheres and cylinders, Phys. Rev. E 39 (1989) 5280–5288.
[37] J. Rubinstein, P. Sternberg, J.B. Keller, Fast reaction, slow diffusion, and curve shortening, SIAM J. Appl. Math. 49 (1989) 116–133.
[38] U. Seifert, Adhesion of vesicles in two dimensions, Phys. Rev. A 43 (1991) 6803–6814.
[39] U. Seifert, Curvature-induced lateral phase segregation in two-component vesicles, Phys. Rev. Lett. 70 (1993) 1335–1338.
[40] H.M. Soner, Convergence of the phase-field equations to the Mullins–Sekerka problem with kinetic undercooling, in: Fundamental Contributions to the Continuum Theory of Evolving Phase Interfaces in Solids, Springer, Berlin, 1999, pp. 413–471.
[41] J.E. Taylor, J.W. Cahn, Linking anisotropic sharp and diffuse surface motion laws via gradient flows, J. Stat. Phys. 77 (1994) 183–197.
[42] E.M. Toose, B.J. Geurts, J.G.M. Kuerten, A boundary integral method for two-dimensional (non)-Newtonian drops in slow viscous flow, J. Non-Newtonian Fluid Mech. 60 (1995) 129–154.
[43] J. van der Waals, The thermodynamic theory of capillarity under the hypothesis of a continuous density variation, J. Stat. Phys. 20 (1893) 197–244.
[44] T.J. Willmore, Riemannian Geometry, Oxford Science Publications, The Clarendon Press Oxford University Press, New York, 1993.